Biomaterials 35 (2014) 9423–9437

Contents lists available at ScienceDirect

Biomaterials

journal homepage: www.elsevier.com/locate/biomaterials

# A microwell pattern for C17.2 cell aggregate formation with concave cylindrical surface induced cell peeling

Li-Guang Zhang [a], Dong-Huo Zhong [a], Yiguo Zhang [a], Chen-Zhong Li [b], William S. Kisaalita [c], Ze-Zhi Wu [a], *

[a] Key Laboratory of Biorheological Science and Technology of the State Ministry of Education, College of Bioengineering, Chongqing University, Chongqing 400044, PR China
[b] Nanobioengineering/Bioelectronics Laboratory, Department of Biomedical Engineering, Florida International University, Miami, FL 33174, USA
[c] Cellular Bioengineering Laboratory, Faculty of Engineering, University of Georgia, Athens, GA 30602, USA

ARTICLE INFO

*Article history:*
Received 17 July 2014
Accepted 23 July 2014
Available online 15 August 2014

*Keywords:*
Cellular aggregate
Neural stem cell
Three dimensional
Polydimethylsiloxane
Finite element analysis

ABSTRACT

We have developed a polydimethylsiloxane (PDMS) pattern with arrays of microwells for the formation of multicellular aggregates by C17.2 neural stem cells. Upon interfacing with the patterns, the neural stem cells would firstly attach to the microwell sidewalls, forming cellular strips on day 1 after plating. For channel connected microwells, cellular strips on the concave semi-cylindrical sidewall surfaces continued among wells and through channels, followed by strip peeling due to prestress arising from actin filaments and assembly of suspending cellular aggregates within the microwells in the following 1–2 days. Our results also suggested that a small microwell diameter of 80 and 100 μm and a narrow channel width of 20 μm would facilitate the aggregate formation among the structural dimensions tested. Finite element method (FEM) simulation revealed that cellular strips on the semi-cylindrical sidewall surfaces peeled under significantly smaller prestresses (critical peeling prestress, CPP), than cells on flat substrates. However, the CPP by itself failed to fully account for the difference in aggregate inducing capability among the patterns addressed, suggesting cell growth behaviors might play a role. This study thus justified the current patterning method as a unique and practical approach for establishing 3D neural stem cell-based assay platforms.

## 1. Introduction

Three-dimensional (3D) cell culture is superior to regular two-dimensional (2D) culture for both basic biological researches and cell-based drug discovery [1], due to the fact that 3D cultures can provide a physiologically more relevant microenvironment and cells therein can more closely recapitulate the *in vivo* functionality and responses [2]. To establish a 3D culture microenvironment, diversified methods are now available where efforts have been focused on the creation of *in vitro* prototype tissues to achieve 3D cell–cell interactions. Multicellular aggregates are a representative example of the *in vitro* prototype tissues underlying most 3D culture approaches and have found a broad range of applications in stem cell biology [3,4], tissue engineering or regenerative medicine [5], experimental oncology [6–8] and other fields. For neural cell-based assays and drug discovery, multicellular neural spheroids have been considered a useful bridge to and even *in vivo* surrogates of animal models [9]. However, successful realization of the potential advantages of cellular aggregates depends, to a large extent, on the development of practical cultivation platforms that are cost effective, compatible with current cell-based assay modalities and easy to control the formation and growth of aggregates under regular culture and medium handling conditions.

Although the culture of cellular aggregates have been well developed for biological research and tissue engineering purposes, translation of the aggregates and scaling down to meet the requirements of cell-based assays are actually challenging. For example, with the traditional hanging drops method [10] or the rotating-wall vessel bioreactors [11], a large number of aggregates can be achieved for most cell types within days of culture with possibly core necrosis or apoptosis associated with oversized aggregates, in addition to non-uniform population expansion and joining among spheroids [6,11,12]. Translation of the aggregates is usually time and reagent consuming, and results in inevitable cell loss. As a result, changes in the number of aggregates available on

---

* Corresponding author. Tel./fax: +86 23 6510 2507.
*E-mail address:* zzwu@cqu.edu.cn (Z.-Z. Wu).

http://dx.doi.org/10.1016/j.biomaterials.2014.07.046
0142-9612/© 2014 Elsevier Ltd. All rights reserved.

the assay platform and non-uniform aggregate sizes and structures may compromise the accuracy of the screening process and complicate the results interpretation.

A possible solution for the cell or aggregate loss and spheroid size non-uniformity in cell-based assays would be the culture of aggregates on porous scaffolds or topographically patterned substrates, where aggregate size distribution will be determined mainly by the pore geometry of the scaffolds or substrates. Also, the strong interaction between aggregates and the scaffolds or substrates will provide mechanical support [13] for the spheroids to withstand forces of medium handling and thus prevent cell loss during the culture and assay processes. However, contrary to this reasoning, the interaction of tumor cell aggregates or stem cell spheroids with artificial substrates and scaffolds usually resulted in phenotypic changes as exemplified by loss of tumor malignancy [8,12] and uncontrolled stem cell differentiation [5]. For embryonic stem cells, such undesired differentiation has been well contained by a feeder layer or suspending culture [3,4,10,14]. For assays with neural stem cell spheroids, a compromise between mechanical support by substrates and undesired differentiation induced by cell-substrate interaction, however, remains a challenge.

Microwell arrays are a prospective powerful cell-based assay platform that is cost effective and compatible with the current fluorescence based screening devices. Early studies in this subfield have taken the advantages of this patterned substrate for trapping and accommodating single isolated cells for high throughput screening [15]. In recent years, microwell arrays have been adopted for the culture of cellular aggregates, with the expectation of good maneuverability and excellent control over the spheroid size and structure with the microwell geometries [14,16,17]. However, in most circumstances the formation of these aggregates relied mainly on natural sedimentation or accumulation of cells onto the well bottoms [14,16]. In case of cells with strong substrate attachment, de-adhesion agents have been added to reduce substrate adhesion and enable cell sedimentation and aggregate formation [17,18]. The major problems pertaining to the sedimentation based aggregate formation are the restriction on mass diffusion as exemplified by inefficiency in nutrient access, waste removal and fluorescence staining, due to failure in establishing aggregate suspension. Li et al. [6] have recently developed a macrowell (in millimeters) based tumor multicellular spheroid culture system, where aggregates were prevented from settling down onto the well bottom by embedding into a hydrogel contained in the wells. However, gel based culture approaches may even compound the diffusion restriction or fluorescence staining inefficiency [19].

It has been reported in recent years that when cells were cultured on a concave grooved surface, the cell bodies might peel from the substrate and form a bridge-like suspension with the proceeding of culture [20–22]. We suppose this was caused by cell contraction in connection with the myosin-driven actin filaments retrograde flow [23], and the redistribution of adhesion complexes [24]. Inspired by this cell behavior and our previous works with microwell patterns [25,26], we have tried to improve our microwell culture platform to establish a 3D multicellular neural spheroid culture approach with patterns of microwell arrays. We reasoned that, by introduction of channel connection to microwell patterns, a microwell would be divided into two semi-cylindrical concave surfaces, geometrically resembling those concave grooved culture substrates. When neural stem cells were cultured with these channel connected microwells and attached on the sidewalls, the adherent cells would eventually peel with the proceeding of culture and then assemble into suspending aggregates supported by tethering to the pattern. This is a complete self-assembly process enabling cellular aggregate formation by substrate anchoring neural stem cells, and is potentially a good way for formation of "well" controlled suspending cellular aggregates with mechanical support even by other cell types characterized by anchorage dependent growth.

Based on the above hypothesis, we have fabricated a polydimethylsiloxane (PDMS) microwell pattern either with or without channel connection, using UV lithography, chemical wet etching and replica molding based soft lithography. C17.2 neural stem cells were interfaced with the microwell pattern for evaluating the aggregate formation capability of the patterned substrates. C17.2 cells were a typical anchorage dependent growth neural stem cell line and have not been reported to form neural spheroids spontaneously under regular 2D culture conditions [27]. We used time-lapse phase contrast microscopy, laser scanning confocal microscopy and scanning electron microscopy to monitor the process of neural spheroids formation on our microwell patterns and then analyzed the aggregate formation efficiency with respect to geometric dimensions of the pattern. For an understanding of the cell mechanics underlying aggregate formation on the microwell patterns, a finite element method (FEM) analysis was performed, using the standard linear solid model [28,29] and the cohesive zone model [30–33], to find out the prestress levels when cell peeling initiated. These simulations were initially carried out with the "best" values for the cell mechanical stiffness and then, the effects of changes in cell instantaneous elastic modulus and adhesion interface elastic modulus on cell peeling were further discussed.

## 2. Materials and methods

### 2.1. Pattern design and fabrication

To achieve efficient cell interfacing, and for an understanding of the impact of channel structure on aggregate formation efficacy, our patterns were basically composed of arrayed microwells, either with or without channel connection (Fig. 1). These patterns had a nominal microwell diameter of 80, 100 and 120 μm, with or without channels of 20 and 40 μm in width, and the microwell depths were 100 μm. For patterns with channel connection, the design of five well units made it easy to stabilize the pattern structures as the microwells were fabricated all the way through to the underlying glass substrates, as well as to locate cells in the subsequent studies. In the following sections of this paper, these patterns will be referred to by "microwell diameter (*D*)"–"channel width (*W*)", e.g., D100-W20 pattern, which indicates that the pattern had a microwell diameter of 100 μm and a channel width of 20 μm. Macroscopically, each pattern structure dimension was designed with a square die in an area of 1 cm × 1 cm, and a total of 9 pattern dimensions or dies were arranged on a quartz–chrome mask, with help from Institute of Microelectronics, Chinese Academy of Sciences (Beijing, China). We used UV lithography, chemical wet etching and replica molding to fabricate the microwell patterns with PDMS (Fig. 1). The silicon master mold was made with a p-type <100> silicon wafer with a resistivity of 7–13 Ω cm (GRINM Semiconductor Materials, Beijing, China). Briefly, the master mold was produced by the following steps: thermal surface oxidation, photoresist coating, UV lithography and development, wet etching in hydrofluoric acid and BOSCH process based dry etching. The silicon master was then silanized with 97% Trichloro (1H, 1H, 2H, 2H-perfluorooctyl) silane (Sigma–Aldrich, USA) for 30 min under vacuum to enable subsequent release of the PDMS mold. The PDMS (Sylgard 184, Dow Corning, USA) prepolymer and the curing agent were extensively mixed in a mass ratio of 10:1, vacuum degassed and poured over the silicon master mold. Samples were vacuum degassed again before cured at 50 °C for 3 h. After cooling, the PDMS patterns were released. We also fabricated flat PDMS substrates following identical steps, except a flat silicon wafer was used instead of the microwell silicon mold.

### 2.2. Cell culture and scanning electron microscopy

C17.2 neural stem cells were routinely maintained in flaks in growth medium at 37 °C in a 5% $CO_2$ humidified incubators. The growth medium was made with Dulbecco's Modified Eagle Medium: Nutrient Mixture F-12 (DMEM/F12, 1:1, Gibco, USA) supplemented with 10% fetal bovine serum (Gibco, USA), 100 U/mL penicillin and 100 μg/mL streptomycin (Sigma–Aldrich, USA). PDMS microwell patterns or flat PDMS substrates were plasma etched for 1 min, sterilized with 70% alcohol under UV light overnight and then placed in a 35 mm Petri dish followed by coating with 0.05 mg/mL polylysine for 2 h. Patterns or flat substrates in dishes were seeded with C17.2 cells at a density of $1 \times 10^5$ cells/mL in the growth medium, 5 mL for each dish, before culture in the incubator. To ensure that we were observing the continuous process of cellular strip formation, strip peeling and aggregate assembly, a series of

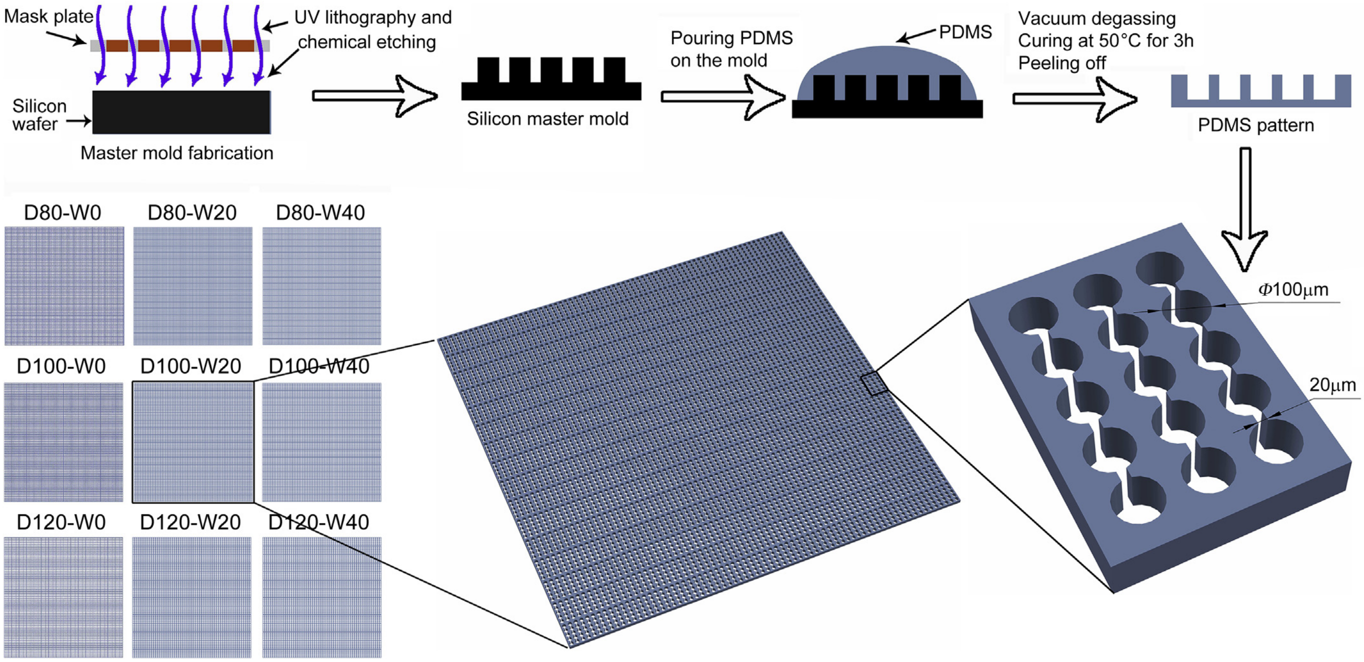

**Fig. 1.** Schematic illustration of the protocols for fabricating the PDMS microwell patterns. Each pattern was designed as a square die of 1 cm in side length. The numbers on the dies or patterns mean "microwell diameter (D)"-"channel width (W)" (μm) and "W0" refers to patterns without channel connection. The right 3D schematic shows the D100-W20 pattern, where five microwells were connected with a channel to form a unit of the array.

time-lapse micrographs for cells on the D100-W20 pattern were taken on days 1, 2 and 4 after plating by a phase contrast microscope (CKX41, Olympus, Japan).

For scanning electron microscopy, cells cultured for 1, 2 and 4 days on microwell patterns were fixed with 2% glutaraldehyde in 0.1 M sodium cacodylate buffer (pH 7.2) for 1 h before rinsing in cacodylate buffer (without glutaraldehyde, pH 7.2) three times, 15 min each. This was followed by 0.9% sodium chloride rinsing twice, 6 min each. The samples were dehydrated sequentially in 30%, 50%, 70%, 80%, 95% and 100% ethanol twice for 5 min each time. Then 50%, 70%, 90%, 95% and 100% of t-butyl alcohol were used to rinse the samples twice, 5 min each. The samples were sputter-coated with gold for 3–5 times, 20 s each. SEM images were then captured with a scanning electron microscope (S-3400N, HITACHI, Japan) at an acceleration voltage of 15 kV.

### 2.3. *Characterization of cell population expansion*

Cells were seeded at a density of $1 \times 10^5$ cells/mL in 35 mm Petri dishes containing a flat PDMS substrate or a microwell patterned substrate, 5 mL for each dish. After 1, 2 and 4 days of culture with growth medium, cells were washed with phosphate buffered saline (PBS) three times and then fixed with PBS containing 40 g/L polyformaldehyde at room temperature for 30 min. Samples were permeabilized with 0.5% Triton-X100 in PBS at room temperature for 10 min and washed in PBS for 3 times. This was followed by nucleus staining with 1 μg/mL 4′,6-diamidino-2-phenylindole (DAPI, Invitrogen, USA) in PBS for 15 min. Patterns were scanned with a confocal laser scanning microscopic system (LSM 510 META, Zeiss, Germany) along the microwell depth from the bottom to the top in a step of 4.14 μm. Imaris software was used to construct the cell nuclei images (volume rendering) and to analyze the number and distribution of cells inside microwells. For statistical comparison, the middle three microwells of the five well units were chosen and cells therein counted. A total of 9 microwells were analyzed for each sample. Cells on flat substrates were counted in a circular area with a diameter of 100 μm. Three independent experiments were done for each substrate. Cell numbers on flat substrates and in microwells on days 1, 2 and 4 were analyzed to evaluate the effects of substrate structure on cell proliferation. In doing this, we analyzed two factors, the structural configuration and culture time, with two-way ANOVA using SPSS 19.0 (IBM, USA). Matlab (MathWorks, USA) was used to fit cell numbers with an exponential equation: $F(t) = Ae^{kt}$, where $k$ is the growth rate, $A$ is the number of cells at the start of the counting (in this case, on day 1 after plating), $F(t)$ is the cell number when the cells were cultured for additional time $t$ after initial counting. The cell doubling time ($DT$) was then calculated according to the definition of $DT$: $F(t + DT) = 2F(t)$.

### 2.4. *Characterization of cellular aggregate formation*

C17.2 cells in the exponentially growing phase were made into suspension with growth medium. After centrifugation and removal of supernatant, cells were suspended in 2 mL carboxyfluorescein diacetate succinimidyl ester (CFSE, Molecular Probes, USA) solution in a concentration of 2 μmol/L. Samples were stained at 37 °C for 30 min, then centrifuged again to remove the unused CFSE. Cells were resuspended in growth medium at a density of $1 \times 10^5$ cells/mL. The suspension was then plated onto patterns of different structural dimensions (either with or without channel connection) contained in Petri dishes, 5 mL for each. On days 1, 2 and 4 after cell plating, cells on the pattern were multi-slice imaged with the confocal laser scanning microscopy system, as outlined in Section 2.3. Three independent repeats were done for each timed sampling.

To quantitatively describe the aggregate formation behavior, we analyzed the middle three microwells of the channel connected five well units, which were found to possibly form cellular aggregates in contrast to the wells at the two ends of the units. If fluorescence of cells was observed along the sidewall of a microwell and for patterns with channel connection, the fluorescence on the two opposing semi-cylindrical sidewall surfaces joined at the position of channel connection and continued through the channel with cellular fluorescence in neighboring wells, this microwell would be referred to as a microwell with cellular strips (MWCS). An MWCS suggested that C17.2 cells in the well had connected to each other and formed cellular strips attaching on the sidewalls and, for channel connected microwells, passing through the connecting channels. If cellular strips in a microwell had detached from the sidewall, and strips from the opposing semi-cylindrical surfaces even assembled to become small cellular clumps, within the well, this microwell would be referred to as a microwell with a cellular aggregate (MWCA). An MWCA suggested initiation or even accomplishment of the assembly of a suspending cellular aggregate in the microwell. Because the presence or absence of an aggregate (or a peeling strip per definition) could be coded as the binary variable: 1 = presence and 0 = absence, logistic regression analysis was used to analyze the data with SPSS [34]. In doing this, whether a microwell was an MWCA or not was entered as the dependent variable, and the cell culture time, microwell diameter and channel width were entered as covariates.

Furthermore, in order to obtain the height distribution of the cellular aggregates in microwells, we delineated the CFSE fluorescence profile of the cellular aggregate for each MWCA. The *Z*-axis position related fluorescence intensities of these profiles were analyzed with Gaussian fitting by Origin 8.0 (Origin Lab Corporation, USA). The aggregate heights were then obtained accordingly based on the peak fluorescence intensities. The data with different culture days and patterns were all processed, and then analyzed with ANOVA and Student's *t*-test.

### 2.5. *Immunofluorescence*

On day 2 after plating, C17.2 cells on the PDMS flat substrates and D100-W20 microwell patterns were used for F-actin and vinculin immunofluorescence staining. Cells were washed with PBS twice, fixed with 4% paraformaldehyde in PBS for 10 min and permeabilized with 0.1% Triton-X100 (Sigma–Aldrich, USA) in PBS at room temperature for 10 min. This was followed by blocking with 10% goat serum in PBS for 15 min. Samples were then incubated overnight at 4 °C in PBS containing FITC–conjugated Phalloidin (1:200, Sigma–Aldrich, USA) and mouse anti-vinculin monoclonal antibody (1:200, Santa, USA). The samples were washed twice in PBS again and then incubated for 1 h at 37 °C with TRITC-conjugated goat anti-mouse IgG (1:100, Santa, USA). The nuclei were stained with 1 μg/mL DAPI (Invitrogen, USA) for 10 min. Fluorescence images of F-actin, vinculin and nuclei were obtained using a confocal microscopic system (Leica SP5, Germany) and an inverted fluorescence microscope (Leica DMI 6000, Germany).

### 2.6. *Simulation of the peeling of cellular strips*

We used FEM to simulate the process of detachment or peeling of cellular strips with ABAQUS 6.9 software (Dassault Systèmes Simulia Corp., USA). By observing the growth of C17.2 cells in the microwells, we found that cells would first adhere to each other and become cellular strips along the sidewall surfaces of the microwell array. For patterns with channel connection, these strips continued among microwells through the connecting channels followed by detachment or peeling of the strips from the sidewall and assembling to form aggregates, along with population expansion (see the Results and Discussion section). To analyze the strip peeling processes in the channel connected microwells, we simplified and modeled this multicellular strip as a single strip composed of the model cellular material (orange), which adhered on a PDMS microwell model (light blue) as shown in Fig. 2a. The two poles of the model cellular strip within the microwell were assumed to be fixed with respect to the XZ plane in the channel, due to the connection or continuation of strips from neighboring microwells therein. Because of the symmetry of the cellular strip and sidewall with respect to the middle of the microwell, it will be reasonable to assume that the cellular strip in the microwell bear the same tractions from the poles in the opposite connecting channels. For an understanding of the effects of pattern geometric dimension on strip peeling and thus aggregate formation, all the six patterns with channel connection involved in this study were modeled, among which the modeling of the D100-W20 pattern was shown in Fig. 2a. As a comparison, we also established a 2D model composed of a round cell spreading on the PDMS flat substrate (Fig. 2b). The model cellular strip for the microwell patterns had a width of 31.0 μm, a thickness of 7.4 μm, and the position or height of the strip on the sidewall was 66.5 μm above the well bottom. The model cell on the flat substrates had a diameter of 36.9 μm and a thickness of 5.5 μm. These parameters were derived from the fluorescence volume rendering results (see Subsection 3.3).

The cells and the pattern substrates in the models were meshed with 4-node tetrahedral elements and 8-node hexahedral elements, respectively. Smaller elements, 1 μm for the microwell model and 0.5 μm for the flat substrate model, were used in the regions of peeling initiation to increase the accuracy of the simulation. The use of even smaller elements had no significant influence on the results of the simulations. The standard linear solid model was used to represent the viscoelastic behavior of the cellular strip in the microwell and the attaching cell on the flat substrate (Supplementary Note 1). The receptor-ligand bonds at the cell-substrate interface were simulated using the bilinear cohesive zone model (Supplementary Note 2). PDMS substrates were modeled as an elastic material with a Young's modulus of 750 kPa and a Poisson's ratio of 0.49. Detailed attributes of cells were shown in Table 1.

**Table 1**
Parameters for FEM simulations with C17.2 neural stem cells.

| Parameter description | "Best" value for C17.2 | Reported range | References |
|---|---|---|---|
| Cell instantaneous elastic modulus (Pa) | 200 | 25–5000[a] | [28,29,35–38] |
| Cell long-term elastic modulus (Pa) | 50 | 5–500[a] | [28,29,35–37] |
| Cell viscosity (kPa·s) | 5 | 0.005–10[a] | [28,29,35–37] |
| Poisson's ratio of the cell | 0.49 | 0.3–0.5 | [36,39] |
| Cell prestress (Pa) | 1000 | 300–25,000 | [40–43] |
| Adhesion interface thickness[b] (nm) | 15 | 10–100 | [33,44–46] |
| Adhesion interface elastic modulus (Pa) | 50 | 1–10,000 | [33,41,42,44,47–50] |

[a] Most of the data were obtained from experiments based on the standard linear solid model.
[b] Namely, the unstressed bond length.

For the simulation, we initially loaded an isotropic prestress of 1000 Pa on cells at the start of simulation to simulate the preexisting tension of the actin filaments. Then the prestress was linearly ramped over time throughout the simulation process, and thus the loading prestress value could be ascertained at any time after initial loading. With the ramping of prestress, we reached the prestress value where peeling of the cell or cellular strip initiated. This prestress value was defined as critical peeling prestress (CPP). CPPs provide a quantitative measure of the level of easiness with which detachment or peeling would occur. The larger the CPP, the more difficultly the cellular strip would peel from the substrate, and vice versa. After obtaining the CPPs, we also established a percent peeled elements *vs.* prestress relation in the simulation, which helped understanding the peeling behavior of cellular strips on the patterns with specific structural dimension or the flat substrates. The "best" values of the attributes that were estimated to be most suitable for simulation with C17.2 cells were listed in Table 1.

## 3. Results and discussion

### 3.1. *Pattern fabrication and cell interfacing*

With a lithography-based replica molding method, we have successfully fabricated PDMS microwell patterns and achieved interfacing of C17.2 neural stem cells for the development of multicellular aggregates-based assay platforms. Similar approaches were also well tailored for stem cell biology researches [14,16–18] and tissue engineering practices [51], where microwells served to provide space for localized cell expansion and assembly into tissues

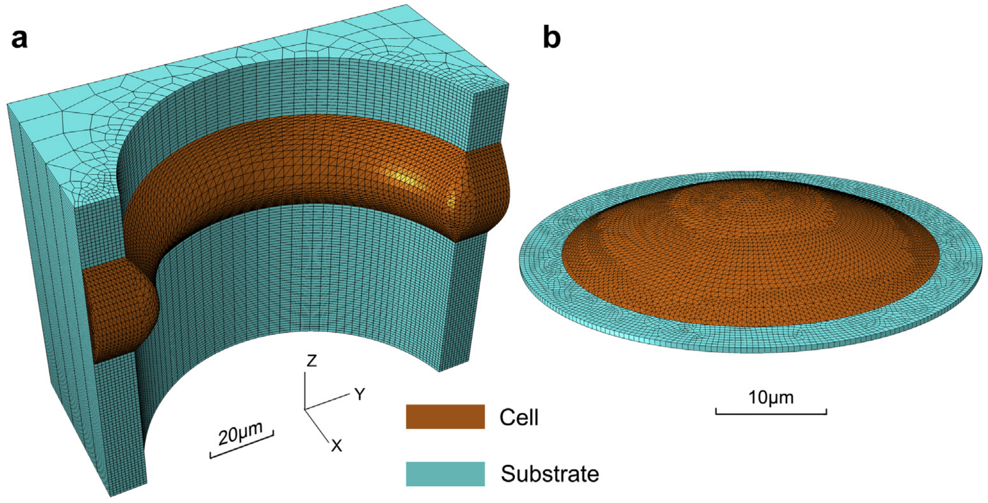

**Fig. 2.** Finite element models with meshing. The light blue denotes the PDMS microwells or flat substrates while the orange the attaching cell or cellular strip. (a) and (b) show modeling of the D100-W20 microwell pattern and the flat substrates, respectively. (For interpretation of the references to color in this figure legend, the reader is referred to the web version of this article.)

when implanted. In order to evaluate the effects of introduction of channel connection and, for neuronal extension guidance in future studies, our microwell patterns were designed both with and without channels. Also, to ensure that we would find the most favorable patterns for 3D aggregate formation, graded geometric dimensions with well diameters of 80, 100, and 120 μm, and channel widths of 0 (no channel connection), 20 and 40 μm were designed, and thus nine patterns were obtained. The design of these dimensions was based on previous studies with SU-8 microwell patterns [25] in which smaller microwells of 50 μm were found ineffective for cell interfacing. Also, it was reported that cells could span across the groove with a width of up to 2–3 times the diameter of the cell body [20,21], which was comparable to the present semi-cylindrical concave "groove" of the microwells. Our ongoing investigations indicate that this protocol also works well for the fabrication of patterns with biodegradable polymers, like poly (L-lactic acid) [26] and poly (DL-lactide-co-glycolide) [52], where patterns were further replica molded from the PDMS mold with excellent control over geometric dimensions.

Fig. 3a shows C17.2 cells cultured on a flat PDMS substrate on day 1 after plating. The cells were polygonous, fully spreading, with few neuronal extensions but numerous lamellipodia, similar to those growing in regular Petri dishes. Fig. 3b shows cells cultured on the D100-W0 pattern for 4 days. From the figure, we found that cells were almost fully attaching on the sidewalls, without aggregate formation. We observed the process of aggregate formation by C17.2 cells within channel connected microwells through time-lapse phase contrast imaging with the D100-W20 pattern when cells were cultured for 1, 2 and 4 days (Fig. 3c). Typically, most of the cells had attached to the sidewall surfaces on day 1 after plating, extending along the circumferential direction and adhering to each other to become multicellular strips in the microwells (Fig. 3c). On day 2 after cell plating, the cellular strip detached from the sidewall gradually, and the cellular strips peeled from the two opposite semi-cylindrical surfaces then came towards the middle of the microwells and assembled to form aggregates until day 4 after plating (Fig. 3c, for a view of cell growth and aggregate formation on the microwell array as a whole, images with lower magnification were shown in Supplementary Fig. 1). These steps typically occurred with the middle 3 wells of the five well units, leading to the aggregate formation, but rarely occurred with the end wells of the unit. This formed the basis for further study on the aggregate formation efficiency where aggregates were observed and counted with the middle 3 microwells. The process of aggregate formation by C17.2 cells was further demonstrated with SEM images, as shown in Fig. 3d, where the typical stages of strip formation, peeling from the sidewalls and aggregate assembly could be clearly distinguished, in more details, for cultures on days 1, 2 and 4 after plating. Fig. 3 c and d also showed that cellular aggregates formed by C17.2 cells were suspending in the microwells by tethering, without attaching to the bottom surface.

In interfacing cells with fabricated substrates, the biological behavior of cells can be significantly affected by the addition of micro and nano features on the substrates, such as microwells, microchannels, ridges and nano roughness [53,54]. For a patterned substrate, these features can be well represented by the structural configuration. Upon cell interfacing, we found that the cells on the concave cylindrical sidewall surface would spread along the surface curvature, thereby facilitating the formation of cellular strips. We speculate that it was due to the cylindrical concave surface which affects the arrangement of the cytoskeleton and the direction of cell pseudopodia extension [55,56]. While the underlying mechanisms remain to be elucidated, the opposite has been found in the case of contact guidance by the cylindrical convex surface of similar curvature where the cells spread along the longitudinal direction rather than along the surface curvature or the circumferential direction [57]. In this regard, more detailed studies are needed.

Our results with microwell patterns also showed that the introduction of channel connection had a profound impact on the formation of cellular aggregates in the microwells. At an initial plating density of $1 \times 10^5$ cells/mL, we found no significant aggregate formation in microwells without channel connection until day 4 after plating while, under the same plating and culture condition, multicellular aggregates were readily observed in channel connected microwells. Considering the alignment of the cellular strips in the microwells and channels, it will be reasonable to speculate that the continuation of the strip and thus the cytoskeletal prestress among microwells and through the connecting channel might be the critical factor in enabling strip peeling and thus aggregate formation. This continuation of cellular strip and cytoskeletal prestress provided an effective mechanical support for cell peeling, because cellular strips within the middle wells of the channel connected microwell units were thus connected to and pulled by the cellular strips in the neighboring microwells. This continuation of strip structure and cytoskeletal prestress was also well evidenced by the mechanical tethering of aggregates after

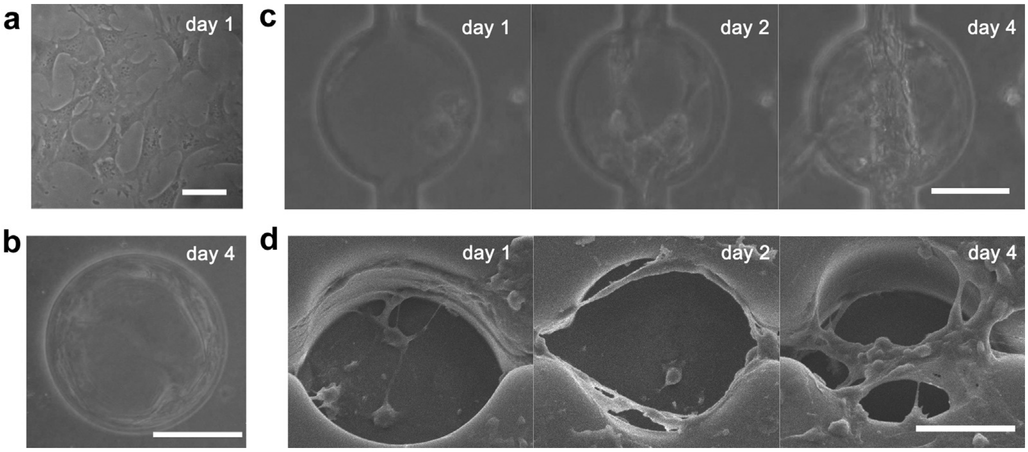

**Fig. 3.** C17.2 neural stem cells cultured on PDMS flat substrates and microwell patterns. Images (a–c) are phase contrast micrographs. (a) Cells cultured on a PDMS flat substrate on day 1 after plating. (b) Cells interfaced with the D100-W0 pattern on day 4 after plating. (c) Time-lapse micrographs for cells interfaced with the D100-W20 pattern on days 1, 2 and 4 after plating. (d) Sequence of SEM images showing the process of multicellular aggregate formation on the indicated days after plating in a microwell of the D100-W20 pattern. Patterns were referred to by well diameter (*D*)–channel width (*W*) in micrometers. Scale bars: 50 μm.

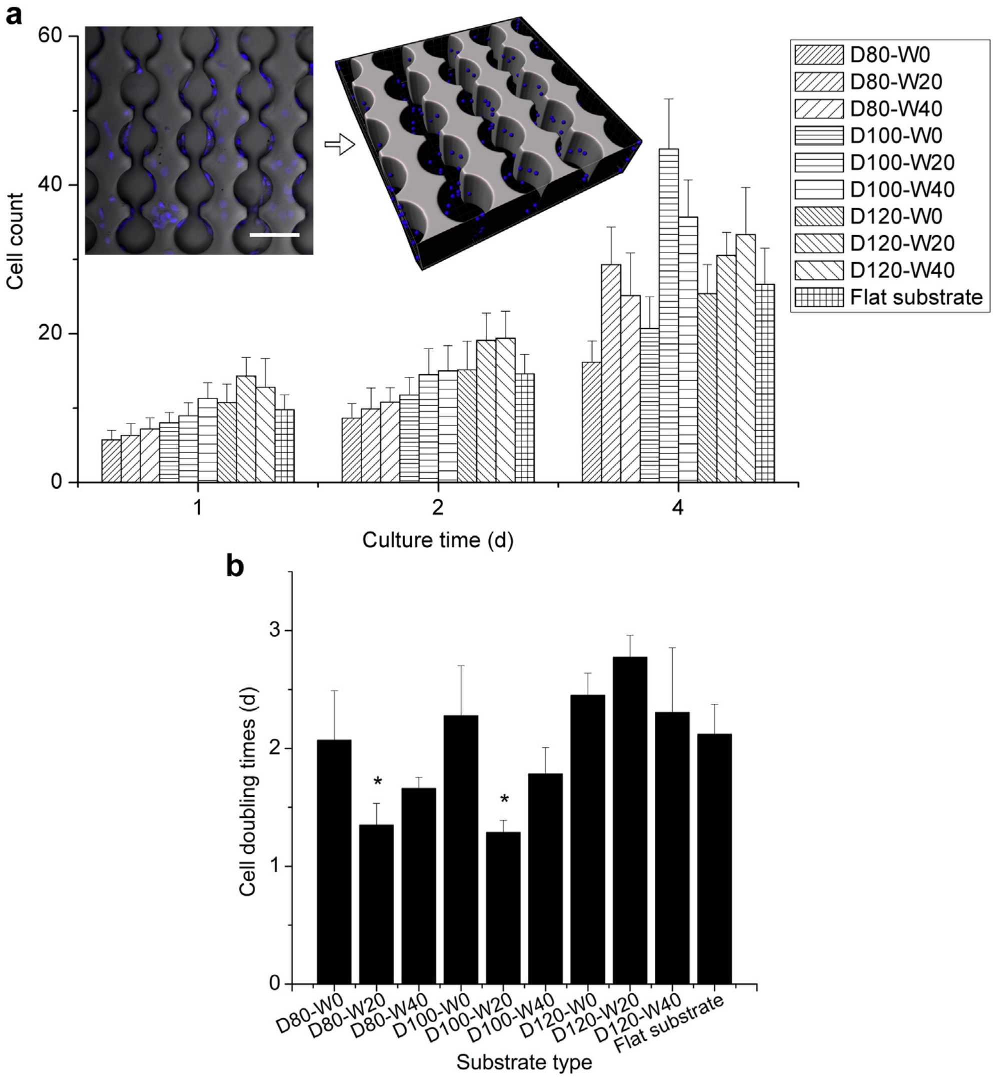

**Fig. 4.** Population expansion of C17.2 cells on PDMS flat substrates and in microwells. (a) Counts of C17.2 cells on flat substrates and in microwells on days 1, 2 and 4 after plating ($n = 3$ experiments; error bars are s.d.). Cells on flat substrates were counted within a circular area of 100 μm in diameter. Cells in microwells were counted with the middle three wells of channel-connected five well units after multi-slice scanning with confocal microscopy and volume rendering with the Imaris software. A total of 9 microwells were analyzed for each pattern, and the counting was expressed as cell number/per microwell. The insets show an example of the volume rendered nuclei distribution on the W80-D20 pattern. Scale bar: 100 μm. (b) Cell number doubling times for the flat substrates and microwell patterns. By Student's *t*-test, the doubling times for the D80-W20 and D100-W20 patterns were compared with those for other substrates ($^*p < 0.05$; $n = 3$ experiments; error bars are s.d.). Patterns were referred to by well diameter ($D$)–channel width ($W$) in micrometers.

strip peeling, which supported the suspending growth of aggregates (Fig. 3 c and d). And for end microwells of the five well units or wells without a channel connection, such mechanical support was actually lacking. It should be noted that reports also appeared that aggregates could form in microwells with no channel connection at a comparably high cell plating density (more than $1 \times 10^6$ cells/mL) [14]. This is understandable in that the structural effects might be greatly obscured or compromised at such high plating densities and the aggregates were actually simple sedimentation and accumulation of cells from the bottom up. In this case, depth or core necrosis and apoptosis were usually expected with long culture times.

C17.2 neural stem cells are an immortalized cell line [27], which was generated by transferring retrovirus-mediated v-myc gene into murine cerebellar progenitor cells. This cell line has been recognized as an excellent model cell for studies of neural stem cell biology, tissue engineering and cell based assays [58,59]. However, as for most anchorage dependent cells, cellular aggregates are not readily achievable for C17.2 neural stem cells under regular culture conditions. In this paper, we have tried a unique approach for inducing aggregate formation by C17.2 neural stem cells by means of concave cylindrical surface induced detachment or peeling with a specific microwell pattern. The immediate advantage of this approach is the ease with which to control aggregate size scale. Uniformity in aggregate size scale will prevent the adverse effects of oversized aggregates like core necrosis and apoptosis. Also, suspending 3D cellular aggregates will be achievable with tethering, thus having efficient mechanical support by the substrates [13]. We believe the current approach will be easily extended to other anchoring cell types, if culture of aggregates is expected, in applications such as 3D co-culture [14] and *in vitro* niche establishment [60].

### 3.2. Characterization of cell population expansion

We quantitatively characterized the population expansion of the interfaced C17.2 cells in our microwell patterns to further understand the effects of the pattern structure on cell growth behavior. To obtain accurate cell numbers in microwells, we stained the nuclei with DAPI, multi-slice scanned the cells by laser scanning confocal microscopy and then analyzed the images to obtain the cell counts and distribution in microwells with the Imaris software. This avoids the problem of overlapping in the *z*-axis and obscuring of the nuclei images under regular fluorescent microscopy.

Fig. 4a shows the number of cells on the flat substrates within a circular area of 100 μm in diameter and in the microwells of the nine patterns on days 1, 2 and 4 after plating. We find that there was a tendency towards an increase in cell numbers with increasing microwell diameter, and larger diameters usually associated with higher numbers of cells in the microwells, on day 1 after cell plating. With the proceeding of culture, cell numbers either on the flat substrates or in the microwells of the 9 patterns increased on days 2 and 4 after plating. To evaluate the relevance of substrate structure to cell population expansion, we first performed a two-way ANOVA analysis to ascertain whether substrate structural characteristics, i.e., flat substrates *vs.* microwell patterns, well diameter, channel connection presence and channel width, have an effect on the cell counts for the substrates. The structural configuration and the culture time were defined as two factors for two-way ANOVA. Results showed that the factors of structural configuration ($F = 29.3$, $p < 0.001$) and culture time ($F = 679.3$, $p < 0.001$) both have significant effects on the cell counts when the analysis included all the ten substrates. As shown in the previous subsection, there was no observable aggregate formation with flat substrates and patterns without channel connection. We thus performed additional ANOVA analysis with the six remaining microwell patterns which had channel connection and were capable of inducing aggregate formation. Again, we found that factors of both structural configuration ($F = 22.8$, $p < 0.001$) and culture time ($F = 478.3$, $p < 0.001$) had significant impact on the cell counts.

To clarify that the difference in cell counts among the patterns was an effect on cell growth or population expansion, which may otherwise be explained by merely plating efficiency, we also obtained the cell population doubling times by assuming an exponential population expansion process. From Fig. 4b, we found that doubling times for cells on flat substrates and in microwells ranged from less than 1.5 days to nearly 3 days. Doubling times for cells on flat substrates were not different from those for the D80-W0, D100-W0, D100-W40, D120-W0 and D120-W40 patterns ($p > 0.05$), but were higher than those for the D80-W20, D80-W40 and D100-W20 patterns ($p < 0.05$) and lower than that for D120-W20 pattern ($p < 0.05$). Among all the patterns and flat substrates, the D80-W20 μm and 100-20 μm patterns were the most favorable patterns for promoting population expansion (within the wells), with the lowest doubling times than any other pattern or the flat substrate ($p < 0.05$). These results confirmed that substrate structure and structural dimensions had significant effects on cell population expansion, and this in turn might impact the formation of multicellular aggregates within microwells of the patterns (see the following Subsection).

One may be concerned that cells would migrate across the boundary of the counting area on flat substrates or across the opening of the microwells, and might thus affect the results of the current experiments. However, due to the fact that the migration was mutual and involved only small number of cells in comparison with the bulk population, we believe that this systematic error will not compromise our conclusion on the impact of substrate or pattern structures on cell population expansion.

### 3.3. *Characterization of the aggregate formation by C17.2 cells with respect to pattern structure and geometric dimensions*

We next characterized the multicellular aggregate formation with respect to the pattern structure and structural dimensions, because the whole process of strip arrangement, strip peeling and aggregate assembly was readily and only observed for microwell patterns (with channel connection) but not flat PDMS substrates. Such analysis will not only enable the design of practical pattern structures for efficient cultivation of aggregates for drugs and toxicity screening, but also reveal the aggregate formation details for, and thus justify the FEM simulation for understanding the underlying mechanisms in terms of cell mechanics. We first characterized the distribution of cellular strips and aggregates within the structures of the patterns. Our previous study suggested that such spatial location or distribution within the pattern structures had critical effects on cellular functionality when neural cells were interfaced with microwell patterns [26].

To enable a 3D localization and to prevent the impact of sample processing, like fixation, on our observation, we stained the cells with the fluorescent dye CFSE, interfaced the stained cells with microwell patterns before multi-slice scanned with confocal microscopy on days 1, 2 and 4 after cell plating. Fig. 5a shows an overlay of the volume rendered confocal fluorescence image with the phase contrast micrograph for C17.2 cells cultured on the D100-W0 pattern on day 4 after plating. Again, in almost all the microwells, cells were found to grow adhering on the circular sidewall with rarely observable aggregate formation, although cell detachment or peeling could occasionally be noted in some wells. This was true even when the experiment was extended until day 7 after plating (data not shown). Fig. 5b shows the images for CFSE stained cells cultured on the D100-W20 pattern on days 1, 2 and 4 after plating, recapitulating the strip formation, strip peeling and aggregate assembly described earlier based on phase contrast microscopy and scanning electron microscopy. It is worth noting that the two wells at the ends of the five-well units rarely accommodated aggregates under current culture condition, confirming the necessity of two semi-cylindrical concave surfaces for enabling aggregate formation in a microwell. With the optically cross sectional views of the stained cells, the fluorescence distribution and thus roughly the strip dimension can be estimated by manually delineating the fluorescence profile. With volume rendering and fluorescence profiling, we found cellular strips in the D100-W20 pattern on day 1 after plating had a width of 31.3 ± 6.3 μm ($n = 20$) and a thickness of 7.4 ± 1.6 μm ($n = 27$) based on the width across the half maximum fluorescence intensities, and the positions or heights of cellular strips on the sidewall were 66.7 ± 8.6 μm above the well bottom ($n = 16$, see also the evaluation of aggregate heights next). Meanwhile, cells on the flat substrates were found to have an equivalent diameter of 36.9 ± 4.0 μm ($n = 20$, converted from projection areas) and a thickness of 5.5 ± 0.7 μm ($n = 20$). Because distinct aggregates usually followed after strip peeling in our observation and thus the peeling marked the initiation of aggregate assembly, we will include the peeling strips into the category of “aggregates” in our next characterization of the aggregate height distribution and aggregate formation efficiency (see the definition of MWCAs in the Materials and methods section).

With optically cross sectional views of aggregates, we evaluated the positions of the aggregates or peeling strips with respect to the microwell depth. This position will determine the capability of the aggregates to sustain a suspending growth state, which characterize the traditional 3D cell culture approaches, such as those with rotating-wall vessel bioreactors [11], and enable nutrients access and waste drainage through the whole surface of aggregates. The

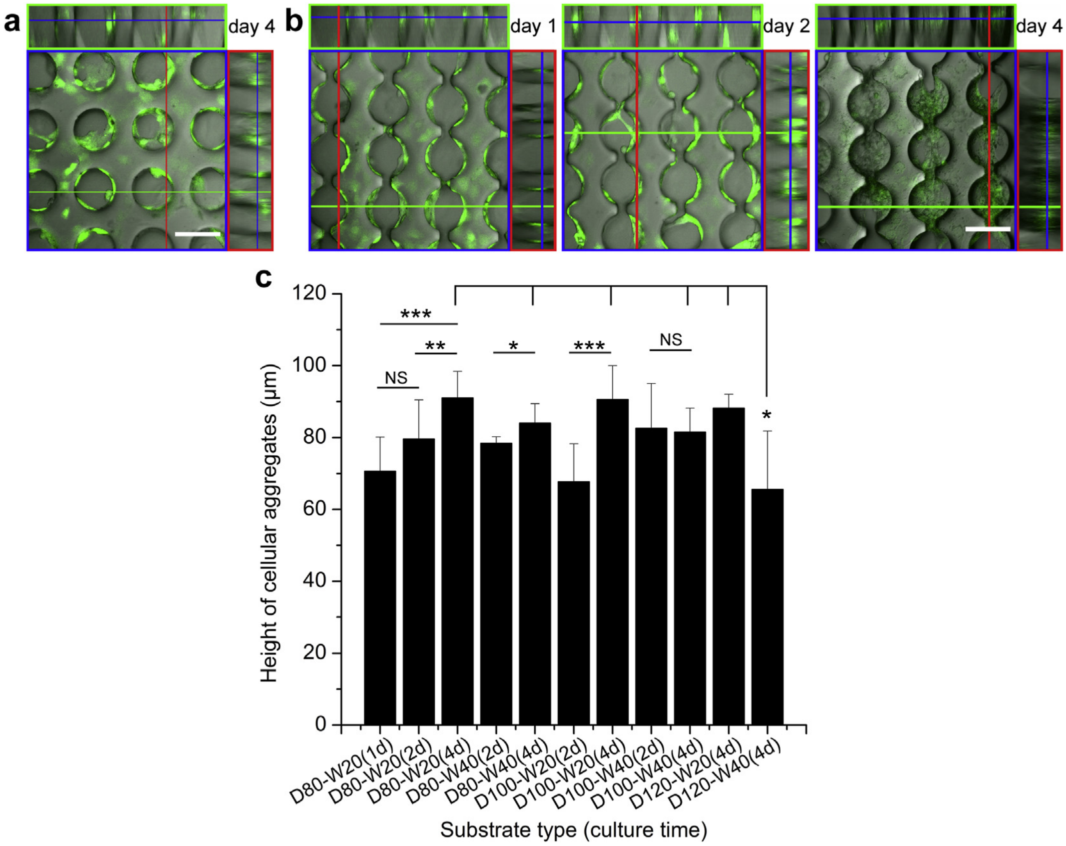

**Fig. 5.** Characterization of the location of the aggregates or peeling strips in microwells. C17.2 cells were stained with CFSE in growth medium and then interfaced with the D100-W0 pattern and cultured until day 4 after plating (a) or with the D100-W20 pattern and cultured until days 1, 2 and 4 after plating (b). Images were obtained by multi-slice scanning with confocal microscopy, volume rendering of the image sequence and overlaying of the confocal fluorescence images with phase contrast micrographs of the patterns. Optically cross sectional views of cells cultured on the patterns were obtained through the indicated colored lines. Scale bars: 100 μm. (c) The positions of the cellular aggregates or peeling strips with respect to the structural depths for all patterns with aggregate formation (with MWCAs). Patterns were represented by microwell diameter (*D*)–channel width (*W*) in micrometers. ($^{*}p < 0.05$, $^{**}p < 0.01$, $^{***}p < 0.001$, NS = non significant; Student's *t*-test, $n = 3$ experiments; error bars are s.d.).

positions of aggregates were analyzed by fitting the fluorescence intensities along the depth of the microwells containing aggregates (MWCAs) with Gaussian distribution, and expressed in terms of locations of the peak fluorescence intensity along the microwell depth. From Fig. 5c, we found that the cellular aggregates formed on our microwell patterns were 60–100 μm above the well bottom. The structure depths of the microwells were around 100 μm. The thickness of the aggregates along the microwell depth was estimated to be 27.7 ± 4.0 μm ($n = 100$), based on the width across the half maximum fluorescence intensities. This suggests that the aggregates were well approaching the microwell opening and our microwell patterns had achieved efficient suspending culture of multicellular aggregates with C17.2 cells, without entailing specific instrumentation like rotating-wall vessel bioreactors.

We hypothesized that the structural dimensions might impact the efficiency of the pattern to support the suspending 3D growth. With ANOVA analysis, we found that these structural dimensions were critical factors in affecting the positions or heights of cellular aggregates within the microwells ($p < 0.001$). Among the aggregates or peeling strips formed, those on the D120-W40 pattern were found to locate at the lowest positions along the microwell depth on day 4 after plating in comparison to those on other patterns ($p < 0.05$). This suggests that the structural dimensions had significant effects on the positions and thus the capability of the pattern to sustain a suspending 3D growth of aggregates within microwells. Aggregates locating at lower positions within the wells might further approach and even attach to the bottom surface for long period of culture due to gravity induced sinking. Our previous study with SH-SY5Y human neuroblastoma cells revealed that locations of neuronal cells within a microwell were related to cell's voltage-gated calcium channel responsiveness and thus the three-dimensionality [26]. These results thus suggest that the design of the structural dimensions offers a practical approach for maintaining three-dimensionality or optimizing cell functionality for cells cultured on a microwell based screening platform.

To characterize the efficiency of the patterns in inducing aggregate formation by C17.2 cells with respect to structural dimensions and thus provide insights for the design of practical assay platforms, we performed a statistical analysis on the rates of aggregate forming wells (MWCAs) for the six patterns having channel connections upon culture of the CFSE stained cells. Within the structural dimensions tested, we found, by student's *t*-test, that a small microwell diameter and a narrow channel width would facilitate the aggregate induction by the pattern, and the D80-W20 and D100-W20 patterns were considered to be the most favorable patterns for aggregate formation by C17.2 cells (Fig. 6 a and b, detailed comparisons among patterns are given in Supplementary Note 3).

To further understand the efficiency of the patterns in inducing aggregate formation by C17.2 cells with respect to structural dimensions, we used binary logistic regression [34] to analyze the data shown in Fig. 6b and obtained the following linear regression equation:

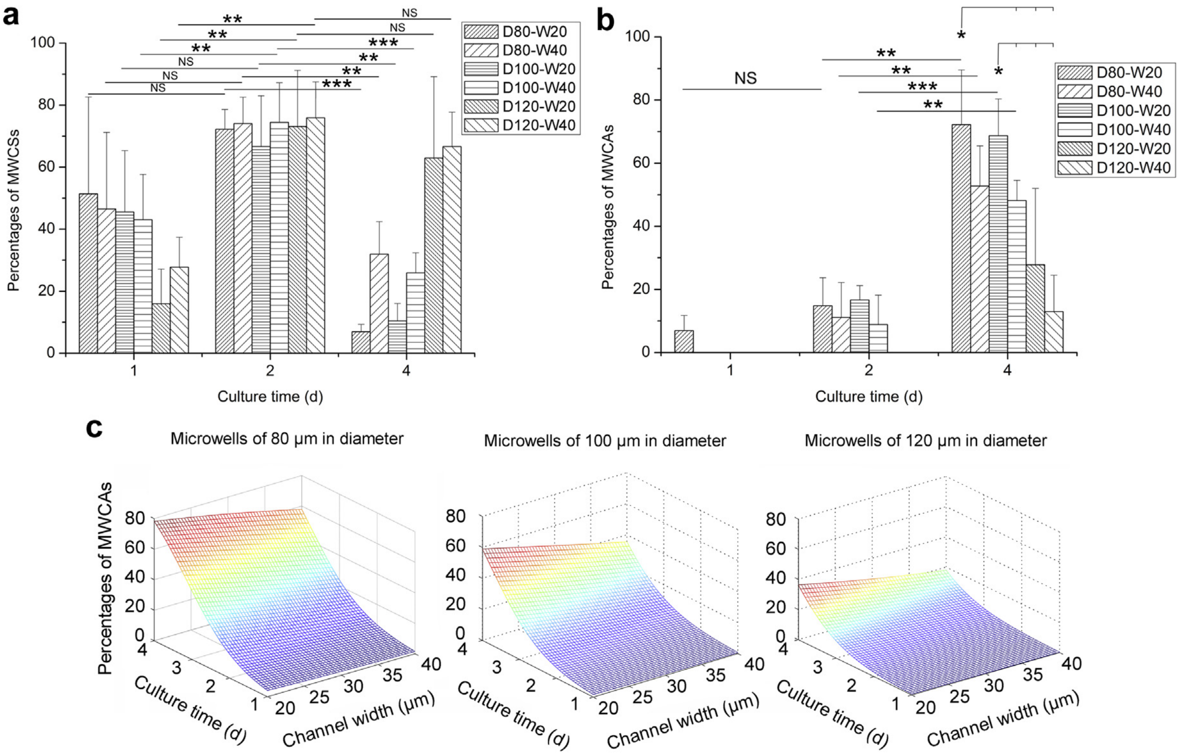

**Fig. 6.** Efficiency of the microwell patterns with channel connection for inducing multicellular aggregate formation by C17.2 neural stem cells. (a, b) Percentages of MWCSs and MWCAs among all pattern wells counted with respect to structural dimensions (well diameters and channel widths) and culture duration (days into culture). Cellular strips or aggregates were identified by volume rendering following multi-slice scanning of the CFSE stained C17.2 cells. ($^*p < 0.05$, $^{**}p < 0.01$, $^{***}p < 0.001$, NS = non significant; Student's *t*-test, $n = 3$ experiments; error bars are s.d.). Patterns were represented by microwell diameter (*D*)–channel width (*W*) in micrometers. (c) Three-dimensional plots of percentages of MWCAs among all pattern wells counted with respect to structural dimensions (well diameters and channel widths) and culture duration (days into culture).

$$\ln\left(\frac{P_A}{1-P_A}\right) = 1.480x_{CT} - 0.046x_{MD} - 0.048x_{CW}, \quad (1)$$

where $P_A$ is the probability of MWCAs, $x_{CT}$, $x_{MD}$ and $x_{CW}$ denote culture time (*d*), microwell diameter (μm) and channel width (μm), respectively. The average prediction accuracy of the regression equation was 86.9% and the *p*-value of the Hosmer–Lemeshow test was 0.359. This suggests that the regression equation thus obtained can well predict the aggregate formation efficiency with respect to pattern structural dimensions under current experimental conditions. Fig. 6c shows 3D plots of percentages of MWCAs with respect to cell culture time and channel width for patterns with a microwell diameter of 80 μm, 100 μm and 120 μm. From Fig. 6c and the coefficients of $x_{CT}$, $x_{MD}$ and $x_{CW}$, it is clear that within the structural dimensions addressed, a small well diameter and a narrow channel width would favor the assembly of 3D cellular aggregates, echoing the conclusion reached with the analysis in Supplementary Note 3. Also, it is understandable that aggregate formation requires a period of culture time for the proceeding of steps of strip formation, strip peeling and aggregate assembly as well as population expansion, and the lengthening of culture time within certain limit will also facilitate this process. However, as has been presented earlier or reported, a microwell diameter below a certain limit will compromise plating efficiency [25] and patterns with channel connection of width zero (without channel connection) will completely prevent aggregate formation. For patterns with a large well diameter (120 μm) or wide connecting channel (40 μm), the low aggregate formation efficiency might be due to failure in either the formation of a fully connected cellular strip or the continuation of cellular prestress through the channels. In this regard, more detailed studies are needed to know the structural limits for the design of practical patterns for efficient culture of neural aggregates.

### 3.4. Immunofluorescence staining for F-actin and vinculin

Under the *in vitro* culture conditions, cell attachment or detachment is largely determined by the adhesive interaction between cell surface receptors and ligand molecules secreted on the substrates, which in turn is strengthened by the focal adhesion plaque assembly and actin filament organization. If the prestress produced by actin-myosin complexes lies within the limit to be balanced by the adhesive interaction, cell attachment would sustain while if this prestress preponderate over the attachment strength, detachment or cell peeling would follow. To further understand the process of strip formation and aggregate initiation at a subcellular or molecular level, we stained the microfilament component F-actin and the focal adhesion marker vinculin for C17.2 cells cultured on either the flat PDMS substrates or the D100-W20 microwell pattern on day 2 after cell plating, as shown in Fig. 7. From the figure, we found that actin filaments could be readily observed in cells cultured on the flat substrates, with a low extent of bundling and lacking a dominant extension direction among cells. For cellular strips within microwells, actin filaments or filament bundles were even more significant than cells on the flat substrates, extending along the curved surface or the circumferential direction and through the channels, similar to the arrangement of cellular strips themselves. These results echoed the observation on the effects of substrate topography on actin filament organization [54], and thus confirmed the continuation of the extension of actin filaments and thus the prestress produced along the curved microwell surface and through the channels of the

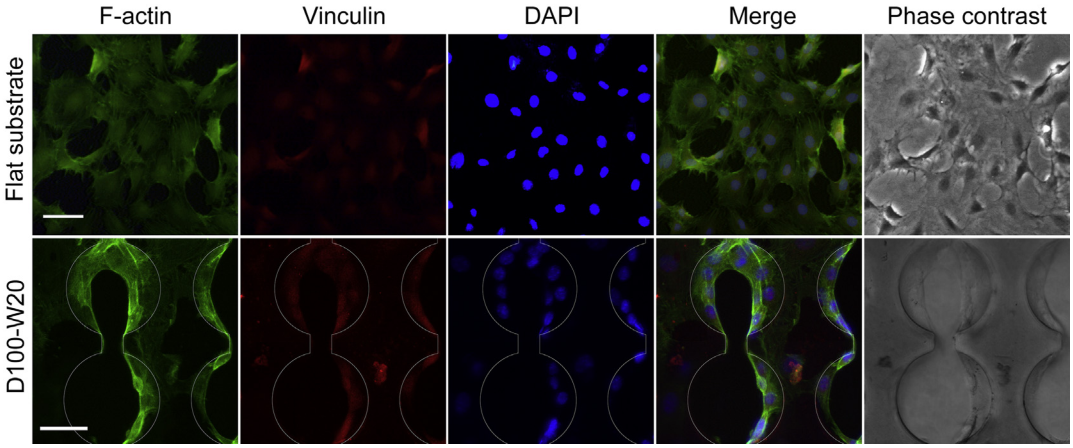

**Fig. 7.** Immunofluorescence staining of C17.2 cells for F-actin and vinculin. Cells were cultured for 2 days on the flat substrates and the D100-W20 pattern. Photos show the F-actin, vinculin, nuclei (DAPI) fluorescences and the merged fluorescence images, as well as the phase contrast micrographs. Scale bars: 50 μm.

pattern. For the vinculin expression, both cells on the flat substrates or within the microwells showed a faint or weak staining without clustering into spots along cell-substrate contacts, suggesting no distinct focal adhesion formation. For cells on the flat substrates, the low extent of microfilament bundling and lack of focal adhesion assembly might be one of the reasons that such neural cells have a small Young's modulus [61].

### 3.5. *FEM simulation of the peeling of cells on the semi-cylindrical concave surfaces vs. flat substrates*

We used FEM to study the process of the multicellular aggregate formation by focusing on the peeling of cellular strips on the semi-cylindrical sidewall surfaces of the microwell patterns *vs.* cells on the flat 2D substrates. In doing this, the standard linear solid model [29,35] was used to describe the viscoelastic behavior of the cells (Supplementary Note 1). The receptor-ligand bonds at the cell-substrate interface were simulated with the bilinear cohesive zone model [30,31](see Supplementary Note 2). We first used the “best” values, which were estimated to be most suitable for simulation with C17.2 cells (Table 1), to simulate with a uniform peeling prestress and cell-substrate interfacial adhesion strength (adhesion interface elastic modulus) by referring to the immunofluorescence staining of actin and vinculin (see the following for explanation). By first modeling with the D100-W20 pattern and the flat substrate (Fig. 2), the percentages of the peeled elements of the adhesion layer with respect to cell prestress levels were obtained (Fig. 8 a and b). Animated videos of the peeling processes are provided as Supplementary Videos 1 and 2. In this case, the CPP for cells on flat substrates was 855.2 Pa (Fig. 8a). For cellular strips on the semi-cylindrical surfaces of the D100-W20 pattern, this value was 389.7 Pa (Fig. 8b), far less than that for cells on flat substrates. This suggests that the C17.2 cellular strips can peel from microwell sidewalls more easily than cells from flat substrates. Two images for the modeling of peeling on flat substrates (insets in Fig. 8a) and four images for modeling with the semi-cylindrical surfaces of the D100-W20 pattern (Fig. 8c) were captured during the simulation. From these images, we found that the strip peeling for modeling with the D100-W20 pattern recapitulated successfully the cellular strip peeling described in Sections 3.1 and 3.3 for C17.2 cells on the same pattern, suggesting our simulations had practical relevance.

Supplementary video related to this article can be found at http://dx.doi.org/10.1016/j.biomaterials.2014.07.046.

We obtained CPPs for strip peeling on the semi-cylindrical sidewalls of all the 6 microwell patterns having channel connections (Fig. 8d). From Fig. 8d, we can find that the CPP values for all the 6 patterns were far less than the corresponding values for cells on flat substrates. However, differences among the CPP values for these 6 patterns were subtle. For patterns with a well diameter of 100 and 120 μm, microwells with a smaller channel width of 20 μm were related to lower CPP values than those with a larger channel width of 40 μm while, on the other hand, the CPP value for the D80-W20 pattern was not less than that for the D80-W40 pattern. For patterns with a channel width of 20 μm, microwells with a larger diameter seem to have lower CPP values, contradicting the expectation with the aggregate formation capabilities observed for these patterns (see Subsection 3.3). These results suggest that the CPP values were relatively insensitive to changes in the pattern structural dimensions addressed in the current research, and differences in CPPs could not fully account for changes in the aggregate inducing capabilities observed among the patterns. For understanding the aggregate inducing capability with respect to pattern structural dimensions, one should be aware that CPPs mark the peeling initiation while other factors like population expansion and aggregates or cellular clumps assembly may also be critical for aggregate formation on the pattern. In this regard, it will be reasonably understandable that the D80-W20 and D100-W20 patterns were the most favorable patterns for both promoting cell population expansion and inducing aggregate formation. Also, small well diameters and channel widths of the pattern will probably favor the formation of cellular strips (Fig. 6a) and the interaction of these strips with the well and channel sidewalls. And this in turn will enable the continuation of cytoskeletal filaments and the resulting prestresses among the wells and through the channels, early in the culture. These factors will all affect the aggregate formation processes, preponderating over or obscuring the effects of CPPs.

In doing the FEM simulation, the smallest mesh size was 0.5 μm, which is orders of magnitude larger than the characteristic length of cell organelles or the minimum spacing (20 nm) of adhesive bonds in the adhesion interface [62], thus justifying the continuum based simulation approach. Our immunofluorescence results showed that the vinculin expression for C17.2 cells either on flat substrates or in microwells was faint and diffuse, suggesting that no mature focal adhesions formed (Fig. 7). In view of this, the possible heterogeneity of the adhesion complex distribution and thus the adhesion interface elastic modulus [33] were ignored in the FEM

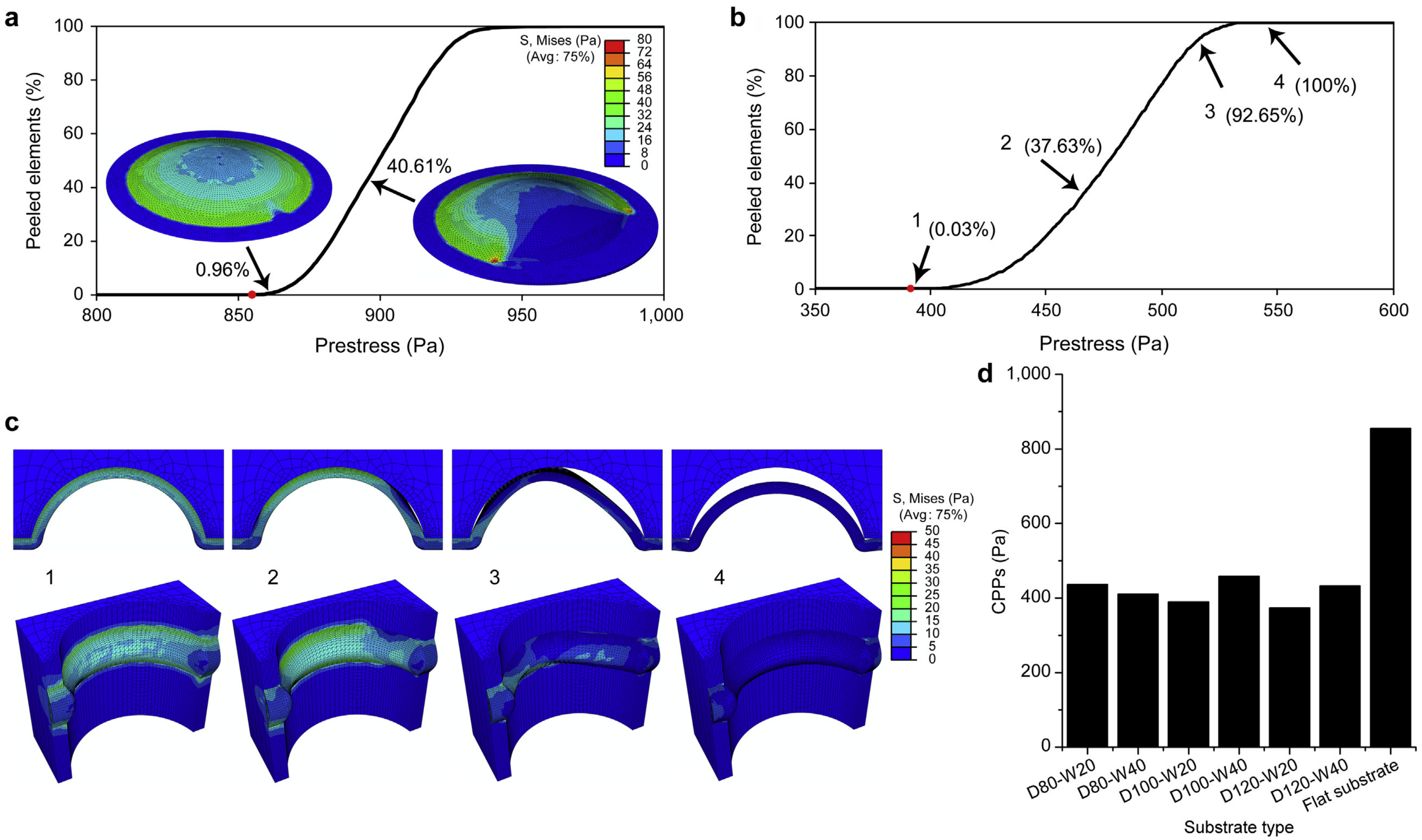

**Fig. 8.** FEM simulation of cell peeling on the flat substrates and microwell patterns that had channel connections. (a) Cell peeling curve showing percent elements of the adhesive interface peeled in relation to cell prestress levels for the flat substrates. The insets show the peeling morphology and the von Mises stress distribution during cell peeling at indicated points on the curve. (b) Cell peeling curve showing percent elements peeled in relation to cell prestress for the D100-W20 microwell pattern. (c) Peeling morphology and the von Mises stress distribution during cell peeling for the D100-W20 microwell pattern at points “1 – 4” shown in (b). The upper panel shows the top plan view while the lower panel the oblique view. Red points in (a) and (b) mark CPP values where peeling initiates. (d) CPPs for the flat substrates and microwell patterns with channel connections. CPP, critical peeling prestress. (For interpretation of the references to color in this figure legend, the reader is referred to the web version of this article.)

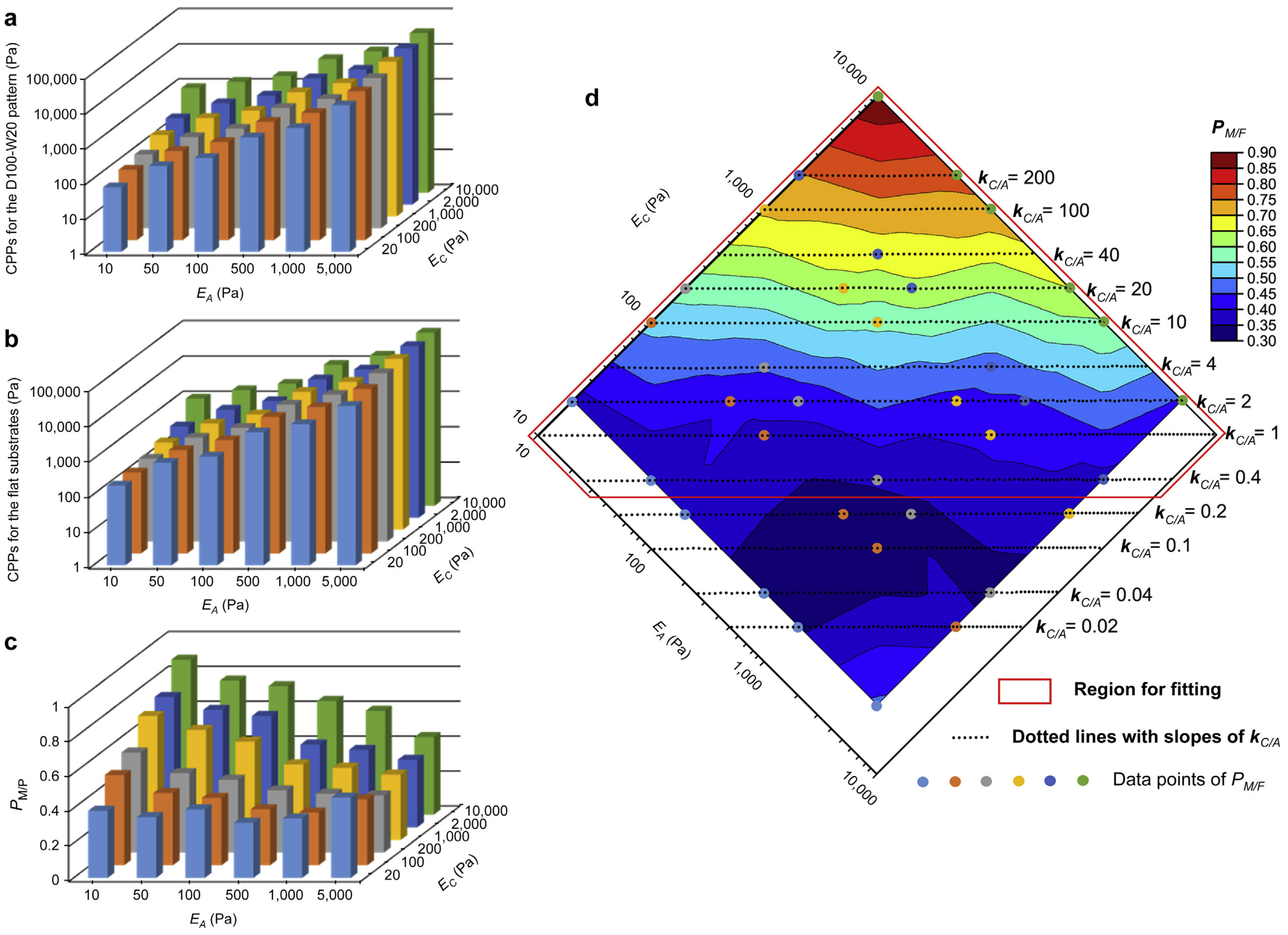

**Fig. 9.** Effects of $E_C$ and $E_A$ on cell peeling. (a–c) show the 3D histograms of peeling stresses with respect to $E_C$ and $E_A$. (a) CPPs for cellular strips on the concave sidewalls of the D100-W20 pattern. (b) CPPs for cells on the flat substrates. (c) $P_{M/F}$, which was defined as the ratio of the CPP for the D100-W20 pattern to that for the flat substrates under the same $E_C$ and $E_A$ values. (d) $P_{M/F}$ in plan view with respect to $E_C$ and $E_A$ on logarithmic coordinates. The background image is a contour plot based on $P_{M/F}$ shown in (c) with linear interpolation. The dotted lines indicative of different slopes or $k_{C/A}$ values were added to show $P_{M/F}$ with respect to $k_{C/A}$. Data points in the red box were used for a linear least-square fit to find out the relationship between $P_{M/F}$ and $k_{C/A}$. CPP, critical peeling prestress. $E_C$, cell instantaneous elastic modulus. $E_A$, adhesion interface elastic modulus. $k_{C/A}$, the ratio of $E_C$ to $E_A$. (For interpretation of the references to color in this figure legend, the reader is referred to the web version of this article.)

simulations. Also, cell or cellular strip peeling was considered similar to the tape peeling described by Ward et al. [63], otherwise fracture of the adhesion complexes should be considered in the simulations in case of significant focal contact formation [33]. Furthermore, as the density of receptor-ligand bonds at the adhesion interface would be in equilibrium within 1 h after cell-substrate contacting [64], the use of a uniform adhesion interface property before and during the cell peeling is reasonable, due to the long time duration of these processes (days) in comparison with that for bond redistribution. The contraction of actin-myosin complexes are the main source of the cell prestress [65]. Immunofluorescence results showed that the actin filaments spread along the circumferential direction of microwell sidewalls (Fig. 7), which indicates that the tension in the circumferential direction may differ from those in other directions. However, actin filaments distributed within C17.2 cells with no predominant direction when cells were cultured on flat substrates. Technically, our simulation had adopted a uniform prestress without counting the ratio of cell tension in different directions, to study the effects of substrate structural configuration on cell peeling behavior. Given the morphology of the cells and the large length to width ratio of the cellular strip on the microwell sidewalls, we believe this simplification will not compromise our conclusion on the peeling of cells on flat substrates and patterns within the structural dimensions addressed.

### 3.6. *Effects of mechanical properties on cell peeling*

So far our simulations have been based on the “best” values for cellular attributes, we now test the effects of changes in these parameters on cell peeling behaviors. Among these attributes, we focused on the cell instantaneous elastic modulus ($E_C$) and adhesion interface elastic modulus ($E_A$), which are the most volatile parameters and may change among cell types and under different culture conditions. $E_C$ values were ramped from 20 to 10,000 Pa while $E_A$ values from 10 to 5000 Pa and the resulting CPPs for cellular strips on the sidewalls of the D100-W20 pattern and cells on the flat substrates were shown in Fig. 9 a and b, respectively. For all the combinations of $E_C$ and $E_A$ values tested, CPPs for flat substrates were higher than those for the D100-W20 pattern, which confirmed the efficacy of the concave sidewall surfaces of the pattern in facilitating cell peeling within a wide range of cell mechanical stiffness. As many anchorage dependent cells (like C17.2 cells) may not peel on flat substrates and CPPs for flat substrates represent the maximum achievable prestresses for adherent cells, a simple CPP ratio ($P_{M/F}$), which was defined as the ratio of the CPP value for the concave sidewall surfaces to that for the flat substrates, was then introduced and calculated (Fig. 9c). This parameter provided a measure for evaluating the level of easiness with which cell peeling or detachment would occur for the microwell pattern. From Fig. 9c, it is evident that $P_{M/F}$ has a negative correlation with $E_A$ but a positive correlation with $E_C$ for most of the ranges tested. This suggests that a small $E_C$ and a large $E_A$ will favor a cellular strip's peeling from the concave sidewall surfaces of the pattern. For adherent cells, there is a positive relationship between $E_C$ and $E_A$ [42]. It will thus be interesting to know the relation of $P_{M/F}$ with respect to $E_C$ and $E_A$.

In dealing this issue, we showed the $P_{M/F}$ data in Fig 9c as a contour plot with linear interpolation (Fig. 9d). Dotted lines with different slopes or $k_{C/A}$ values, which were the ratio of $E_C$ to $E_A$ ($k_{C/A} = E_C/E_A$), were added to show $P_{M/F}$ with respect to $k_{C/A}$. During our simulations, we found when $k_{C/A}$ is less than 0.4, the peeling behaviors of cells or cellular strips would be far different from those observed under actual experimental conditions. This is understandable since it will be hard for a cell or cellular strip to sustain a peeling process similar to the tape peeling described by Ward et al. [63] and fracture of the adhesion complexes [33] may have taken places for a low $k_{C/A}$ or a high $E_A$. In view of this, we selected the $P_{M/F}$ data points in the red box (Fig. 9d, with $k_{C/A}$ larger than 0.4) for a linear least-square fit (3D plot shown in Supplementary Fig. 2), to obtain the following equation:

$$P_{M/F} = 0.3266 + 0.1477 \log k_{C/A} + 0.0279 \log E_C, \tag{2}$$

where $R^2 = 0.9800$. From this equation, one could find that $P_{M/F}$ has a positive correlation with $E_C$ and $k_{C/A}$. When $k_{C/A}$ remains unchanged, $P_{M/F}$ will increase with the increasing of either $E_C$ or $E_A$. Conversely, when $E_C$ or $E_A$ remains unchanged, $P_{M/F}$ will increase with the increasing of $k_{C/A}$.

It will be tempting to extend the current research to other assay platforms by evaluating the peeling capabilities of cells on a curved topographic substrate. The challenge for such assays lies first in the establishment of the physiologically or pathophysiologically relevant substrate topography or curvature with respect to the *in vivo* microenvironments. Also, due to contact inhibition or low cadherin expression by many cell types [26], cellular strips will not be readily achievable and the calculation may thus need to be fine-tuned. In spite of this, due to the relative insensitivity of the CPPs to pattern structural dimensions (see Subsection 3.5), we obtained the $P_{M/F}$ values for a number of cells with Eq. (2) and the $E_C$ and $E_A$ values reported (Supplementary Note 4). We found that the calculated $P_{M/F}$ values were in good agreement with these cells' peeling abilities on the concave substrates. Interestingly, we also found $P_{M/F}$ values may be related to the metastatic potentials of cancer cells (Supplementary Note 4). These results verified the efficiency of our FEM simulations and raised the possibility for the current study to be extended to researches in experimental oncology.

## 4. Conclusion

We have developed a PDMS pattern with arrays of microwells for the formation of multicellular aggregates by C17.2 neural stem cells. The induction of aggregate formation by the pattern takes advantage of cell peeling on concave microwell sidewall surfaces after cellular strip formation. The resulting aggregates were suspending in microwells with tethering to the pattern and thus have effective mechanical support for withstanding regular culture handling. Within the structural dimensions tested, we found that a small microwell diameter and a narrow channel width would facilitate the aggregate induction by the pattern and thus the D80-W20 and D100-W20 patterns were considered to be the most favorable patterns for aggregate formation by C17.2 cells. With the FEM simulation of the peeling process, we found that cellular strips on the semi-cylindrical sidewall surfaces peeled with significantly smaller CPPs than cells on flat substrates. However, the CPP by itself failed to fully account for the difference in aggregate inducing capability among the patterns addressed, suggesting cell growth behaviors might play a role. Insights for the design of practical assay platforms were discussed in terms of pattern structural dimensions and cell mechanical stiffness, especially the cell instantaneous elastic modulus and adhesion interface elastic modulus. This study thus justified the current pattern as a practical approach for establishing 3D neural stem cell-based assay platforms.

## Acknowledgments

This work was supported by the National Natural Science Foundation of China (30870570) and the Foundation for Sci & Tech Research Project of Chongqing (CSTC2009AB5202).

## Appendix A. Supplementary data

Supplementary data related to this article can be found at http://dx.doi.org/10.1016/j.biomaterials.2014.07.046.

## References

[1] Abbott A. Cell culture: biology's new dimension. Nature 2003;424:870–2.
[2] Pampaloni F, Reynaud EG, Stelzer EH. The third dimension bridges the gap between cell culture and live tissue. Nat Rev Mol Cell Biol 2007;8:839–45.
[3] Konno T, Akita K, Kurita K, Ito Y. Formation of embryoid bodies by mouse embryonic stem cells on plastic surfaces. J Biosci Bioeng 2005;100:88–93.
[4] Schulz TC, Palmarini GM, Noggle SA, Weiler DA, Mitalipova MM, Condie BG. Directed neuronal differentiation of human embryonic stem cells. BMC Neurosci 2003;4:27.
[5] Levenberg S, Huang NF, Lavik E, Rogers AB, Itskovitz-Eldor J, Langer R. Differentiation of human embryonic stem cells on three-dimensional polymer scaffolds. Proc Natl Acad Sci U S A 2003;100:12741–6.
[6] Li X, Zhang X, Zhao S, Wang J, Liu G, Du Y. Micro-scaffold array chip for upgrading cell-based high-throughput drug testing to 3D using benchtop equipment. Lab Chip 2014;14:471–81.
[7] Yamada KM, Cukierman E. Modeling tissue morphogenesis and cancer in 3D. Cell 2007;130:601–10.
[8] Zhao Y, Yao R, Ouyang L, Ding H, Zhang T, Zhang K, et al. Three-dimensional printing of Hela cells for cervical tumor model in vitro. Biofabrication 2014;6:035001.
[9] Lai Y, Cheng K, Kisaalita W. Three dimensional neuronal cell cultures more accurately model voltage gated calcium channel functionality in freshly dissected nerve tissue. PLOS ONE 2012;7:e45074.
[10] Yoon BS, Yoo SJ, Lee JE, You S, Lee HT, Yoon HS. Enhanced differentiation of human embryonic stem cells into cardiomyocytes by combining hanging drop culture and 5-azacytidine treatment. Differentiation 2006;74:149–59.
[11] Low HP, Savarese TM, Schwartz WJ. Neural precursor cells form rudimentary tissue-like structures in a rotating-wall vessel bioreactor. In Vitro Cell Dev-an 2001;37:141–7.
[12] Mueller-Klieser W. Tumor biology and experimental therapeutics. Crit Rev Oncol Hematol 2000;36:123–39.
[13] Vogel V, Sheetz M. Local force and geometry sensing regulate cell functions. Nat Rev Mol Cell Biol 2006;7:265–75.
[14] Khademhosseini A, Ferreira L, Blumling 3rd J, Yeh J, Karp JM, Fukuda J, et al. Co-culture of human embryonic stem cells with murine embryonic fibroblasts on microwell-patterned substrates. Biomaterials 2006;27:5968–77.
[15] Rettig JR, Folch A. Large-scale single-cell trapping and imaging using microwell arrays. Anal Chem 2005;77:5628–34.
[16] Moeller HC, Mian MK, Shrivastava S, Chung BG, Khademhosseini A. A microwell array system for stem cell culture. Biomaterials 2008;29:752–63.
[17] Markovitz-Bishitz Y, Tauber Y, Afrimzon E, Zurgil N, Sobolev M, Shafran Y, et al. A polymer microstructure array for the formation, culturing, and high throughput drug screening of breast cancer spheroids. Biomaterials 2010;31:8436–44.
[18] Anada T, Masuda T, Honda Y, Fukuda J, Arai F, Fukuda T, et al. Three-dimensional cell culture device utilizing thin membrane deformation by decompression. Sens Actuators B Chem 2010;147:376–9.
[19] Desai A, Kisaalita WS, Keith C, Wu ZZ. Human neuroblastoma (SH-SY5Y) cell culture and differentiation in 3-D collagen hydrogels for cell-based biosensing. Biosens Bioelectron 2006;21:1483–92.
[20] Goldner JS, Bruder JM, Li G, Gazzola D, Hoffman-Kim D. Neurite bridging across micropatterned grooves. Biomaterials 2006;27:460–72.
[21] Limongi T, Cesca F, Gentile F, Marotta R, Ruffilli R, Barberis A, et al. Nanostructured superhydrophobic substrates trigger the development of 3D neuronal networks. Small 2013;9:402–12.
[22] Nikkhah M, Strobl JS, De Vita R, Agah M. The cytoskeletal organization of breast carcinoma and fibroblast cells inside three dimensional (3-D) isotropic silicon microstructures. Biomaterials 2010;31:4552–61.
[23] Lin C, Espreafico E, Mooseker M, Forscher P. Myosin drives retrograde F-actin flow in neuronal growth cones. Neuron 1996;16:769–82.
[24] Wozniak MA, Modzelewska K, Kwong L, Keely PJ. Focal adhesion regulation of cell behavior. Biochim Biophys Acta 2004;1692:103–19.
[25] Wu ZZ, Zhao Y, Kisaalita WS. Interfacing SH-SY5Y human neuroblastoma cells with SU-8 microstructures. Colloids Surf B 2006;52:14–21.
[26] Wu ZZ, Wang ZW, Zhang LG, An ZX, Zhong DH, Huang QP, et al. Responsiveness of voltage-gated calcium channels in SH-SY5Y human neuroblastoma cells on quasi-three-dimensional micropatterns formed with poly (l-lactic acid). Int J Nanomed 2013;8:93–107.
[27] Snyder EY, Deitcher DL, Walsh C, Arnoldaldea S, Hartwieg EA, Cepko CL. Multipotent neural cell lines can engraft and participate in development of mouse cerebellum. Cell 1992;68:33–51.
[28] Lim CT, Zhou EH, Quek ST. Mechanical models for living cells–a review. J Biomech 2006;39:195–216.
[29] Schmidschonbein GW, Sung KLP, Tozeren H, Skalak R, Chien S. Passive mechanical properties of human leukocytes. Biophys J 1981;36:243–56.
[30] McGarry JP, Murphy BP, McHugh PE. Computational mechanics modelling of cell–substrate contact during cyclic substrate deformation. J Mech Phys Solids 2005;53:2597–637.
[31] Ronan W, Deshpande VS, McMeeking RM, McGarry JP. Numerical investigation of the active role of the actin cytoskeleton in the compression resistance of cells. J Mech Behav Biomed 2012;14:143–57.
[32] Evans EA, Calderwood DA. Forces and bond dynamics in cell adhesion. Science 2007;316:1148–53.
[33] Ward MD, Hammer DA. A theoretical analysis for the effect of focal contact formation on cell-substrate attachment strength. Biophys J 1993;64:936–59.
[34] McLaren CE, Chen WP, Nie K, Su MY. Prediction of malignant breast lesions from MRI features: a comparison of artificial neural network and logistic regression techniques. Acad Radiol 2009;16:842–51.
[35] Wu ZZ, Zhang G, Long M, Wang HB, Song GB, Cai SX. Comparison of the viscoelastic properties of normal hepatocytes and hepatocellular carcinoma cells under cytoskeletal perturbation. Biorheology 2000;37:279–90.
[36] MacQueen LA, Buschmann MD, Wertheimer MR. Mechanical properties of mammalian cells in suspension measured by electro-deformation. J Micromech Microeng 2010;20:065007.
[37] Lu YB, Franze K, Seifert G, Steinhauser C, Kirchhoff F, Wolburg H, et al. Viscoelastic properties of individual glial cells and neurons in the CNS. Proc Natl Acad Sci U S A 2006;103:17759–64.
[38] Spedden E, White JD, Naumova EN, Kaplan DL, Staii C. Elasticity maps of living neurons measured by combined fluorescence and atomic force microscopy. Biophys J 2012;103:868–77.
[39] Barreto S, Clausen CH, Perrault CM, Fletcher DA, Lacroix D. A multi-structural single cell model of force-induced interactions of cytoskeletal components. Biomaterials 2013;34:6119–26.
[40] Wang N, Naruse K, Stamenovic D, Fredberg JJ, Mijailovich SM, Tolic-Norrelykke IM, et al. Mechanical behavior in living cells consistent with the tensegrity model. Proc Natl Acad Sci U S A 2001;98:7765–70.
[41] Ladoux B, Nicolas A. Physically based principles of cell adhesion mechanosensitivity in tissues. Rep Prog Phys 2012;75:116601.
[42] Wang N, Tolic-Norrelykke IM, Chen J, Mijailovich SM, Butler JP, Fredberg JJ, et al. Cell prestress. I. Stiffness and prestress are closely associated in adherent contractile cells. Am J Physiol Cell Physiol 2002;282:C606–16.
[43] Park CY, Tambe D, Alencar AM, Trepat X, Zhou EH, Millet E, et al. Mapping the cytoskeletal prestress. Am J Physiol Cell Physiol 2010;298:C1245–52.
[44] Bell GI, Dembo M, Bongrand P. Cell adhesion – competition between nonspecific repulsion and specific bonding. Biophys J 1984;45:1051–64.
[45] Chen W, Lou J, Evans EA, Zhu C. Observing force-regulated conformational changes and ligand dissociation from a single integrin on cells. J Cell Biol 2012;199:497–512.
[46] Calderwood DA, Campbell ID, Critchley DR. Talins and kindlins: partners in integrin-mediated adhesion. Nat Rev Mol Cell Biol 2013;14:503–17.
[47] Qin TW, Yang ZM, Wu ZZ, Xie HQ, Qin J, Cai SX. Adhesion strength of human tenocytes to extracellular matrix component-modified poly(DL-lactide-co-glycolide) substrates. Biomaterials 2005;26:6635–42.
[48] Moore SW, Roca-Cusachs P, Sheetz MP. Stretchy proteins on stretchy substrates: the important elements of integrin-mediated rigidity sensing. Dev Cell 2010;19:194–206.
[49] Shi P, Shen K, Ghassemi S, Hone J, Kam LC. Dynamic force generation by neural stem cells. Cell Mol Bioeng 2009;2:464–74.
[50] Koch D, Rosoff WJ, Jiang J, Geller HM, Urbach JS. Strength in the periphery: growth cone biomechanics and substrate rigidity response in peripheral and central nervous system neurons. Biophys J 2012;102:452–60.
[51] Kato-Negishi M, Tsuda Y, Onoe H, Takeuchi S. A neurospheroid network-stamping method for neural transplantation to the brain. Biomaterials 2010;31:8939–45.
[52] Zhang LG, Wu ZZ, Song ZQ, Huang QP, Liao YJ, Li CZ. Fabrication of three-dimensional microwell patterns and their integration with C17.2 neural stem cells. Shengwu yixue gongchengxue zazhi (in Chinese) 2012;29:555–62.
[53] Martinez E, Engel E, Planell JA, Samitier J. Effects of artificial micro- and nano-structured surfaces on cell behaviour. Ann Anat 2009;191:126–35.
[54] Ochsner M, Dusseiller MR, Grandin HM, Luna-Morris S, Textor M, Vogel V, et al. Micro-well arrays for 3D shape control and high resolution analysis of single cells. Lab Chip 2007;7:1074–7.
[55] Parker KK, Brock AL, Brangwynne C, Mannix RJ, Wang N, Ostuni E, et al. Directional control of lamellipodia extension by constraining cell shape and orienting cell tractional forces. Faseb J 2002:16.
[56] Choi CK, Vicente-Manzanares M, Zareno J, Whitmore LA, Mogilner A, Horwitz AR. Actin and alpha-actinin orchestrate the assembly and maturation of nascent adhesions in a myosin II motor-independent manner. Nat Cell Biol 2008;10. 1039–U36.
[57] Svitkina TM, Rovensky YA, Bershadsky AD, Vasiliev JM. Transverse pattern of microfilament bundles induced in epitheliocytes by cylindrical substrata. J Cell Sci 1995;108:735–45.
[58] Park KI, Teng YD, Snyder EY. The injured brain interacts reciprocally with neural stem cells supported by scaffolds to reconstitute lost tissue. Nat Biotechnol 2002;20:1111–7.
[59] Yang F, Murugan R, Wang S, Ramakrishna S. Electrospinning of nano/micro scale poly(L-lactic acid) aligned fibers and their potential in neural tissue engineering. Biomaterials 2005;26:2603–10.

[60] Gobaa S, Hoehnel S, Roccio M, Negro A, Kobel S, Lutolf MP. Artificial niche microarrays for probing single stem cell fate in high throughput. Nat Methods 2011;8:949–55.

[61] Engler AJ, Sen S, Sweeney HL, Discher DE. Matrix elasticity directs stem cell lineage specification. Cell 2006;126:677–89.

[62] Patla I, Volberg T, Elad N, Hirschfeld-Warneken V, Grashoff C, Fassler R, et al. Dissecting the molecular architecture of integrin adhesion sites by cryo-electron tomography. Nat Cell Biol 2010;12:909–15.

[63] Ward MD, Dembo M, Hammer DA. Kinetics of cell detachment: effect of ligand density. Ann Biomed Eng 1995;23:322–31.

[64] Tolentino TP, Wu J, Zarnitsyna VI, Fang Y, Dustin ML, Zhu C. Measuring diffusion and binding kinetics by contact area FRAP. Biophys J 2008;95:920–30.

[65] Dowling EP, Ronan W, Ofek G, Deshpande VS, McMeeking RM, Athanasiou KA, et al. The effect of remodelling and contractility of the actin cytoskeleton on the shear resistance of single cells: a computational and experimental investigation. J R Soc Interface 2012;9:3469–79.